Fermi surface reconstruction in electron-doped cuprates without antiferromagnetic long-range order

Junfeng He[a,b], Costel R. Rotundu[a,b,c], Mathias S. Scheurer[d], Yu He[a,b,c], Makoto Hashimoto[e], Ke-Jun Xu[b,c], Yao Wang[a,d], Edwin W. Huang[a,b,f], Tao Jia[a,b,f], Sudi Chen[a,b,c], Brian Moritz[a,b], Donghui Lu[e], Young S. Lee[a,b,c], Thomas P. Devereaux[a,b,g], and Zhi-xun Shen[a,b,c,f,1]

[a]Stanford Institute for Materials and Energy Sciences, SLAC National Accelerator Laboratory, Menlo Park, CA 94025; [b]Geballe Laboratory for Advanced Materials, Stanford University, Stanford, CA 94305; [c]Department of Applied Physics, Stanford University, Stanford, CA 94305; [d]Department of Physics, Harvard University, Cambridge, MA 02138; [e]Stanford Synchrotron Radiation Lightsource, SLAC National Accelerator Laboratory, Menlo Park, CA 94025; [f]Department of Physics, Stanford University, Stanford, CA 94305; and [g]Department of Materials Science and Engineering, Stanford University, Stanford, CA 94305

Contributed by Zhi-xun Shen, December 25, 2018 (sent for review September 19, 2018; reviewed by and Peter Armitage and Louis Taillefer)

Fermi surface (FS) topology is a fundamental property of metals and superconductors. In electron-doped cuprate $Nd_{2-x}Ce_xCuO_4$ (NCCO), an unexpected FS reconstruction has been observed in optimal- and overdoped regime ($x = 0.15$–0.17) by quantum oscillation measurements (QOM). This is all the more puzzling because neutron scattering suggests that the antiferromagnetic (AFM) long-range order, which is believed to reconstruct the FS, vanishes before $x = 0.14$. To reconcile the conflict, a widely discussed external magnetic-field–induced AFM long-range order in QOM explains the FS reconstruction as an extrinsic property. Here, we report angle-resolved photoemission (ARPES) evidence of FS reconstruction in optimal- and overdoped NCCO. The observed FSs are in quantitative agreement with QOM, suggesting an intrinsic FS reconstruction without field. This reconstructed FS, despite its importance as a basis to understand electron-doped cuprates, cannot be explained under the traditional scheme. Furthermore, the energy gap of the reconstruction decreases rapidly near $x = 0.17$ like an order parameter, echoing the quantum critical doping in transport. The totality of the data points to a mysterious order between $x = 0.14$ and 0.17, whose appearance favors the FS reconstruction and disappearance defines the quantum critical doping. A recent topological proposal provides an ansatz for its origin.

high-temperature superconductors | angle-resolved photoemission | quantum critical point | topological order | strongly correlated electrons

Fermi surface topology is the starting point to understand various emergent quantum phenomena in metals, including high-temperature superconductivity. With both momentum and energy resolution, angle-resolved photoemission (ARPES) is an ideal tool to directly reveal the Fermi surface (FS) topology of a material. However, in electron-doped cuprates, a direct understanding of the ARPES results has been limited by the data quality (1–4). This is primarily due to the lack of a large high-quality surface area in a material that is difficult to cleave. Utilizing a recently developed ARPES beam line at Stanford Synchrotron Radiation Lightsource (SSRL) with a small beam spot, we have managed to probe intrinsic electronic structures from a small but uniform region on the cleaved sample surface. This technical advancement leads to a significant improvement on the experimental data quality (*SI Appendix*, Fig. S1) that enables us to quantitatively investigate the FS topology in electron-doped cuprates.

When an FS reconstruction takes place, the energy band is folded with respect to the antiferromagnetic zone boundary (AFMZB) and an energy gap opens up, giving rise to a backbending behavior of the band at the AFMZB (5) (see Fig. 1 *A*–*C* for a schematic diagram). If the gap is below Fermi level (E_F) (Fig. 1*B*), then the E_F cuts through the conduction band, resulting in an electron-like pocket (e.g., antinodal region in Fig. 1*A*). Conversely, if the gap is above E_F (Fig. 1*C*), a hole-like pocket appears on the FS (e.g., nodal region in Fig. 1*A*). On the other hand, when the FS reconstruction is absent (Fig. 1*D*), the electron band disperses continuously, regardless of the AFMZB (Fig. 1 *E* and *F*). Neither band folding nor gap opening is expected.

Earlier ARPES measurements on underdoped samples have revealed the AFM gap (2–7), hints of the folded band (8), and disconnected segments on the FS (2–7), supporting the reconstruction scenario in underdoped regime (2). However, things become more complicated with electron doping (4, 6, 9–11). Photoemission constant-energy map at E_F of the optimal-doped $Nd_{2-x}Ce_xCuO_4$ (NCCO, $x = 0.15$) seems to suggest a large FS centered at (π, π) (4). But, a spectral weight analysis of the nodal dispersion favors a reconstructed FS for the optimal-doped $Sm_{2-x}Ce_xCuO_{4-\delta}$ (SCCO, $x = 0.15$) (10). While slight variations between different material families have been discussed (11), a direct understanding of the FS topology requires a better resolution of the key features—band folding and gap opening at the AFMZB.

Results

With the improved precision of data, our measurements on the optimal-doped NCCO ($x = 0.15$) clearly reveal both band folding and gap opening at the AFMZB (momentum cut near the "hot-spot" where the FS intersects AFMZB, Fig. 1 *G*–*I*), demonstrating the existence of a reconstructed electron-like pocket. The FS

Significance

Fermi surface (FS) topology is a fundamental property of metals and superconductors. In electron-doped cuprate $Nd_{2-x}Ce_xCuO_4$, an unexpected FS reconstruction has been observed in optimal- and overdoped regime ($x = 0.15 - 0.17$) by quantum oscillation measurements (QOM). This is puzzling because neutron scattering suggests that the antiferromagnetic long-range order, which is believed to reconstruct the FS, vanishes before $x = 0.14$. Here, we report angle-resolved photoemission evidence of FS reconstruction. The observed FSs are in quantitative agreement with QOM, suggesting an intrinsic FS reconstruction without field. Furthermore, the energy gap of the reconstruction decreases rapidly near $x = 0.17$ like an order parameter, echoing the quantum critical doping in transport. The totality of the data points to a mysterious order between $x = 0.14$ and 0.17.

Author contributions: J.H. and Z.-x.S. designed research; J.H., C.R.R., M.S.S., Y.H., M.H., K.-J.X., Y.W., E.W.H., T.J., S.C., B.M., D.L., Y.S.L., and T.P.D. performed research; J.H., Y.H., and Z.-x.S. analyzed data; J.H. led the experiment; Z.-x.S. was responsible for the overall project management; and J.H. and Z.-x.S. wrote the paper with input from all authors.

Reviewers: P.A., Johns Hopkins University; and L.T., University of Sherbrooke.

The authors declare no conflict of interest.

[1]To whom correspondence should be addressed. Email: zxshen@stanford.edu.

This article contains supporting information online at www.pnas.org/lookup/suppl/doi:10.1073/pnas.1816121116/-/DCSupplemental.

Published online February 11, 2019.

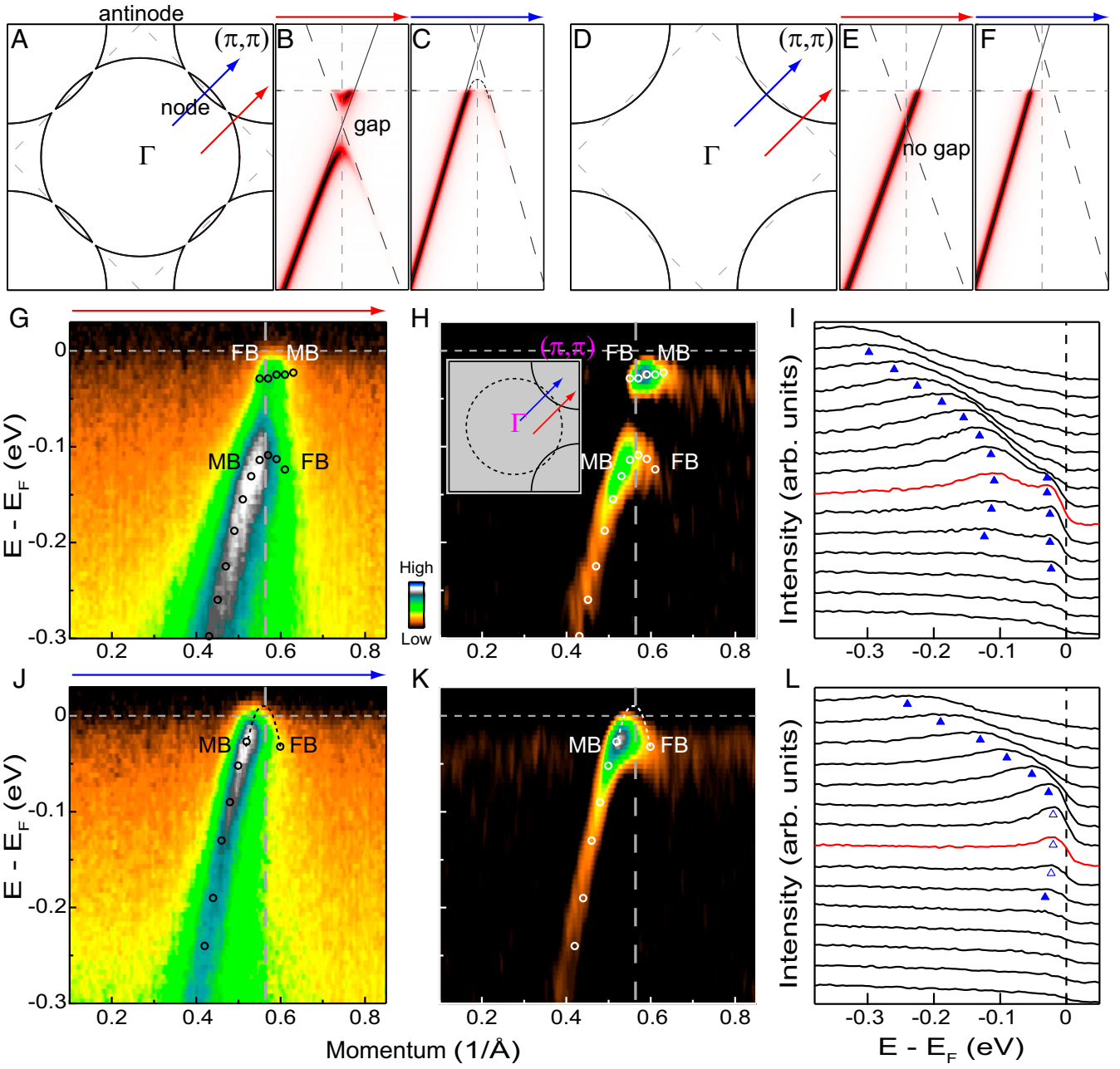

Fig. 1. FS reconstruction in optimal-doped NCCO. (*A*) Schematic diagram of a reconstructed FS with electron-like pockets near the antinode and hole-like pockets near the node. The dashed lines indicate the AFM Brillouin zone. (*B*) Schematic band dispersion along a momentum cut on the electron-like pocket (near hotspot), marked by the red arrow in *A*. The original dispersion is split into conduction- and valence bands by an AFM energy gap. The reconstructed bands bend back at the AFMZB. (*C*) Schematic band dispersion along a momentum cut on the hole-like pocket (nodal cut), marked by the blue arrow in *A*. The AFM energy gap is slightly above E_F, but the folded band (back-bent hole band) disperses below E_F. The gray (dashed) line in *B* and *C* represents the original (folded) band. (*D*–*F*) The same as *A*–*C*, but for the original FS without reconstruction. (*G*–*I*) Photoemission intensity plot (G), second derivative image with respect to energy (*H*) and raw energy distribution curves (EDCs) (*I*) for optimal-doped NCCO, measured along a momentum cut on the electron-like pocket (near hotspot, labeled by the red arrow in *H*, *Inset*). Conduction- and valence bands extracted from the EDCs (blue triangles in *I*) are also presented in *G* (black circles) and *H* (white circles). The EDC at the AFMZB is shown in red (*I*). The main band and folded band are marked by "MB" and "FB," respectively. (*J*–*L*) The same as *G*–*I*, but for the nodal cut (labeled by the blue arrow in *H*, *Inset*).

reconstruction is also supported by the nodal dispersion (Fig. 1 *J*–*L*), where the Fermi level crosses the hole band, forming a hole-like pocket near the node. The possible gap opening above E_F cannot be seen by ARPES, but the back-bending of the hole band (folded band) is discernible (Fig. 1 *J*–*L*). A reconstructed FS should also be accompanied by a hotspot between the electron-like and hole-like pockets, where a gap exists at the Fermi level (Fig. 1*A*). This is also observed in our experiment (see *SI Appendix*, Fig. S2 for the FS mapping and the momentum cut through the hotspot).

After establishing the FS reconstruction in optimal-doped NCCO, we quantitatively investigate the associated energy gap. Surprisingly, the gap shows a strong momentum dependence. An ∼80-meV gap appears near the hotspot (Fig. 2*B*), but it vanishes at the AFMZB near the antinode (Fig. 2 *C* and *H* and *SI Appendix*,

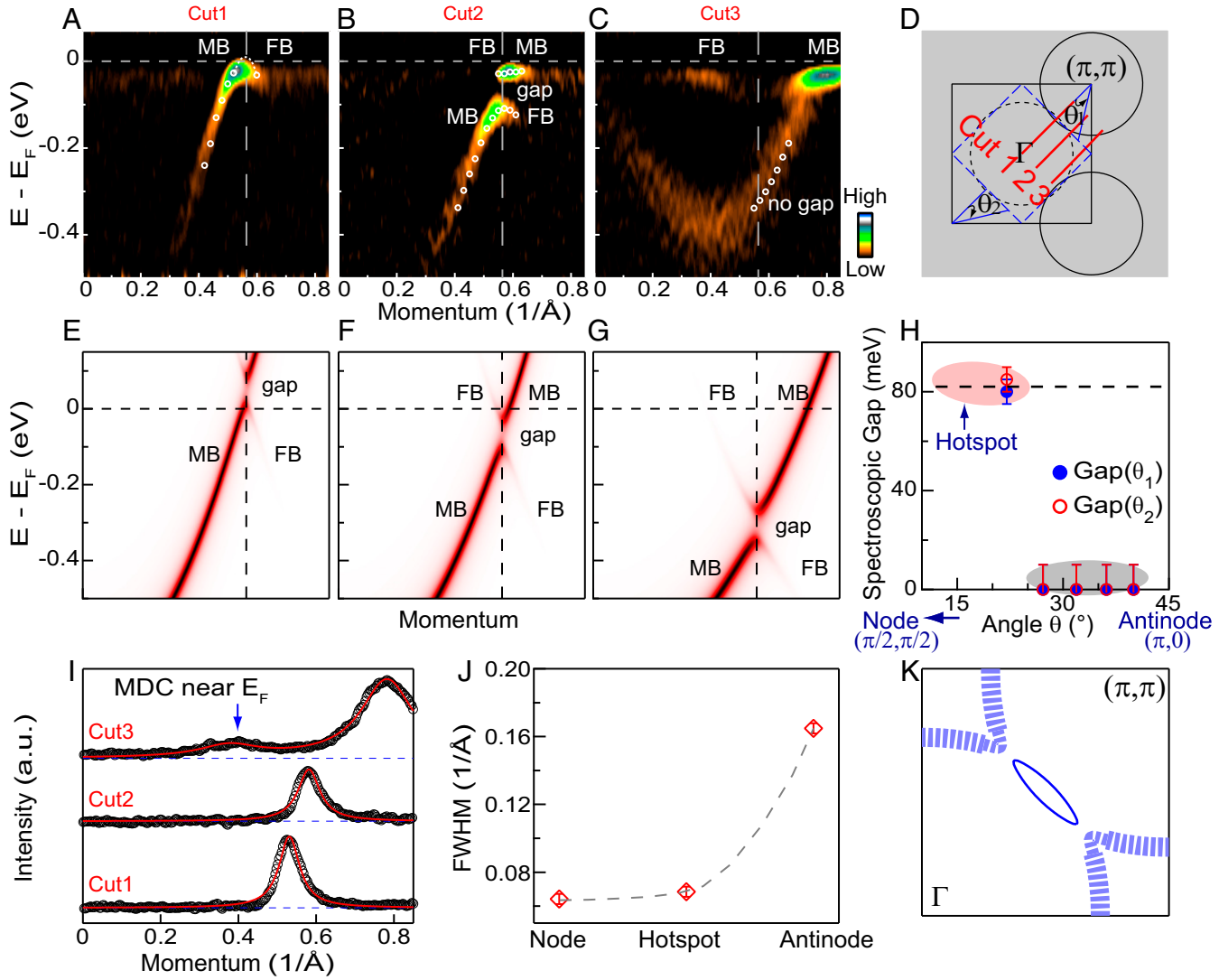

Fig. 2. Momentum-dependent gap in optimal-doped NCCO. (*A–C*) Band dispersion (second derivative image with respect to energy) along three momentum cuts as labeled in *D*. The vertical dashed lines mark the AFMZB. The kink feature (~65 meV) in *C* comes from electron–boson coupling (see *SI Appendix*, Fig. S3 for more details). The main band and folded band are marked by MB and FB, respectively. (*E–G*) Mean-field simulations with a momentum-independent gap of 82 meV. The energy of the intersecting point between the original band and the AFMZB for each spectrum is selected to mimic the experiment. (*H*) Momentum dependence of the measured spectroscopic gap. Note that both intrinsic gap and scattering rate contribute to the spectroscopic gap. We emphasize that the folded conduction band is still clearly observed near the antinode (*C* and *I*), forming the reconstructed electron-like Fermi pocket. (*I*) Integrated MDCs near E_F (−0.03 ~ 0 eV) for the three cuts. The blue arrow marks the MDC peak from the folded band. (*J*) Full width at half maximum extracted from the main MDC peaks in *I*. The error bar comes from the fitting. Note that different slopes of the band dispersion at different momentum locations might also contribute to the change of MDC width near E_F. However, the overall dispersion near the antinode shows a much larger MDC width than that near the node and hotspot, indicating an enhanced scattering rate near the antinode. (*K*) Schematic FS. The blurred electron-like pockets indicate the enhanced scattering rate.

Fig. S3). This is distinct from the mean-field band-folding picture, where a momentum-independent constant energy gap is expected (Fig. 2 *E–G*). To understand the differences, we note that a moderate energy gap can be smeared out on the photoelectron spectra when an enhanced scattering rate takes place (*SI Appendix*, Fig. S4). The measured electron scattering rate, represented by the width of the momentum distribution curves (MDC) near E_F (Fig. 2*I*), does show a substantial momentum dependence (Fig. 2*J*). The enhanced scattering rate near the antinode, when combined with its deep binding energy where the band crosses the AFMZB, could give rise to the folded band without a resolvable gap opening (*SI Appendix*, Fig. S4). As such, the gap itself is likely isotropic and the apparent momentum dependence of the gap in Fig. 2*H* can be attributed to the scattering rate difference. Although the absolute value of scattering rate deduced from ARPES is different from that in transport, the strong momentum dependence coincides with the fact that only the hole-like pocket near the node has been observed in QOM, while the expected electron-like pocket near the antinode is absent (12–17). The origin of the momentum-dependent scattering rate is yet to be understood, where the electron correlation might be at play.

Next, we study the doping dependence of the FS reconstruction. Both the back-bending behavior (folded band) and gap opening have been observed at all doping levels we measured ($x = 0.11, x = 0.15, x = 0.16$), demonstrating that the FS reconstruction persists to the overdoped regime. This is consistent with QOM (12–17), and the well-defined gap suggests that a magnetic breakdown in QOM is less likely below $x = 0.16$. However, the gap decreases rapidly near $x = 0.16$ (Fig. 3*F*), which is consistent with our inability to observe a gap beyond $x = 0.16$. Such a behavior of gap closing near

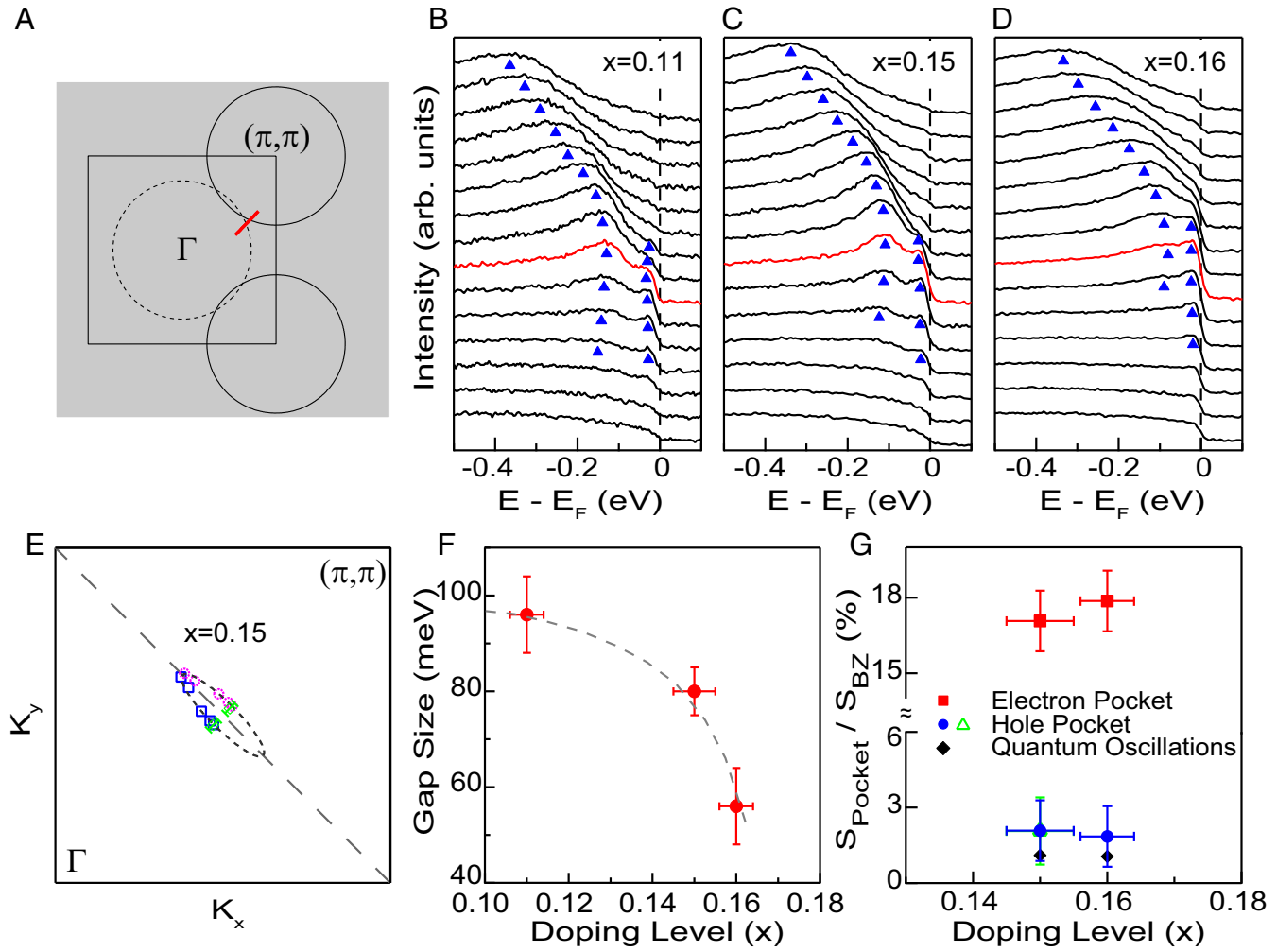

Fig. 3. Doping dependence of the Fermi surface reconstruction. (*B–D*) Raw EDCs for doping levels $x = 0.11$, 0.15, and 0.16 respectively. The corresponding momentum cut is shown in *A*. The EDCs at the AFMZB are shown in red. Note that both back-bending and gap opening appear right at the AFMZB for all doping levels. These key features differentiate FS reconstruction from bosonic mode coupling (see *SI Appendix*, Fig. S3 for details). (*E*) Extracted hole-like Fermi pocket near the node. The green squares represent the Fermi momenta (K_F) extracted from the main band and folded band along the nodal cut. The blue squares mark the K_F obtained from the main band along off-nodal cuts, and the dashed pink circles indicate the folded K_F, which are extracted from the negative branch of the main band and shifted by the wave vector (π, π) (see *SI Appendix*, Fig. S5 for details). The error bar comes from the uncertainty in the determination of K_F. (*F*) Doping dependence of the gap size at the AFMZB, estimated by the energy separation between the valence-band top and conduction-band bottom at the AFMZB, as indicated by the blue triangles on the red EDCs in *B–D*. Vertical error bars here represent uncertainties of the extracted gap size. Horizontal error bars in *F* and *G* represent the uncertainties of the doping levels, determined by EPMA. (*G*) Doping dependence of the Fermi pockets. The red squares (electron-like pocket) and blue circles (hole-like pocket) represent the size of the pockets estimated from the energy gap (*F*). The green triangle (hole-like pocket) shows the value extracted from *E*. The black diamonds are the results from QOM (13). Vertical error bars represent uncertainties of the pocket size.

$x = 0.16$~0.17 is consistent with a quantum critical point (QCP) in that doping range, as suggested by an x to $1–x$ density transition in transport experiments (13, 18, 19). The size of the reconstructed Fermi pockets can also be measured. One way is to directly estimate the area of the pockets via FS mapping (Fig. 3*E* and *SI Appendix*, Fig. S5). Alternatively, one can also estimate the pocket size using the reconstructed band dispersion and the gap size (see *SI Appendix* for details). Both methods give similar results, which are quantitatively consistent with quantum oscillation results as in Fig. 3*G*. The similar Fermi pockets observed by our measurements and QOM indicate the existence of a robust FS reconstruction, regardless of the external magnetic field.

Discussion

One scenario for the ARPES data is a remnant short-range order (8, 20–22). Strictly speaking, a short-range order does not break the global translational symmetry of the crystal. However, it might provide a scattering channel with a wave vector $Q \pm \Delta Q$, where ΔQ is proportional to the inverse of the correlation length, and thus an approximate "FS folding." Nevertheless, with the small AFM correlation length in overdoped NCCO ($x = 0.16$) of ~7 planar lattice constant (23), a weak coupling mean-field simulation does not capture the experimental observations (*SI Appendix*, Fig. S6). Our data, on the other hand, leave room for a strong coupling picture with short-range AFM fluctuation, as those suggested by the Hubbard model calculations. Here the momentum folding remains commensurate with the local correlation at $Q = (\pi, \pi)$, and the gap magnitude is also dominated by the local interaction and thus remains similar in different regions (*SI Appendix*, Fig. S7). Our experimental energy and momentum width allow such a picture. However, it is unclear whether the quantum critical doping, as seen by the rapid decrease of the

energy gap near $x = 0.16$ (Fig. 3*F*) and the corresponding transport data (13, 18, 19, 24–26), can be understood by such a purely local picture without invoking long-range order.

The totality of ARPES, QOM, and transport data suggests the presence of an intrinsic long-range order that persists up to the critical doping near $x = 0.16$–0.17. Long-range AFM order can naturally explain this phenomenology. However, neutron-scattering data from the rod-like magnetic scattering in the bulk indicate the lack of coexistence between long-range AFM order and superconductivity beyond $x = 0.14$ (23). A similar conclusion is drawn by the muon spin rotation measurements on another electron-doped cuprate $La_{2-x}Ce_xCuO_{4-\delta}$, where the static magnetism and superconductivity do not coexist (27). One is therefore left with a puzzle on the origin of the long-range order in our superconducting NCCO samples with $x = 0.15$–0.16 doping.

Charge order has been reported in NCCO (28), but the associated wave vector does not match the observed FS reconstruction. Another possible way out involves topological order that exploits the topological character of the Luttinger theorem (29–31). Without breaking the translational symmetry, the existence of topological order in a state with short-range AFM order can still reconstruct the FS with respect to the AFMZB (29–31) (also see *SI Appendix*, Fig. S8). In such gauge theory, the gauge-dependent Higgs field cannot be directly observed, but can play a role similar to an order parameter. Its presence could have observable consequences like the opening of the gap, which has magnitude related to the local magnetic order and its closing defines a QCP. It would be instructive to have deeper understanding of the transport behavior near a topological QCP for refined comparison with experiment to further test the validity of such ansatz. It would also be interesting to explore whether the same basic scenario can be at play in hole-doped cuprates.

Through much improved experiment, our data have established the intrinsic doping dependence of FS topology in NCCO, and provided a microscopic underpinning for QOM without the need to assume magnetic-field–induced long-range AFM order in the optimal- and overdoped regime. The rapid closing of the gap near $x = 0.16$–0.17 reveals the likely order parameter of the quantum critical doping in transport experiments (13, 18, 19, 24–26). Confronted by the neutron conclusion of an absence of long-range AFM order beyond $x = 0.14$ (23), a correlation driven topological order provides an ansatz to reconcile the dilemma.

Materials and Methods

Samples. Single crystals of NCCO ($x = 0.11$, 0.15, and 0.16) were grown by the traveling-solvent floating-zone method in O_2 and annealed in Ar. The doping levels were determined by electron probe microanalysis (EPMA).

ARPES. ARPES measurements were carried out at beam line 5–2 of the Stanford Synchrotron Radiation Lightsource of SLAC National Accelerator Laboratory with a total energy resolution of ~12 meV and a base pressure better than 5×10^{-11} Torr. The data were collected with 53-eV photons at ~20 K. The Fermi level was referenced to that of a polycrystalline Au film in electrical contact with the sample. The smallest beam spot size at the beam line is ~40 μm (horizontal) × 10 μm (vertical). For our experiments, a beam spot of ~40 μm (horizontal) × 80 μm (vertical) was chosen, which optimized the photoelectron counts on a single uniform surface region.

ACKNOWLEDGMENTS. We thank S. Sachdev, D. J. Scalapino, D.-H. Lee, P. J. Hirschfeld, S. A. Kivelson, J. Zaanen, N. Nagaosa, A. Georges, C. M. Varma, and S. Uchida for useful discussions. The work at SLAC and Stanford University is supported by the US Department of Energy (DOE), Office of Basic Energy Science, Division of Materials Science and Engineering. SSRL is operated by the Office of Basic Energy Sciences, US DOE, under Contract DE-AC02-76SF00515. M.S.S. acknowledges support from the German National Academy of Sciences Leopoldina through Grant LPDS 2016-12. This research used resources of the National Energy Research Scientific Computing Center (NERSC), a US DOE Office of Science User Facility operated under Contract DE-AC02-05CH11231.

1. Damascelli A, Hussain Z, Shen ZX (2003) Angle-resolved photoemission studies of the cuprate superconductors. *Rev Mod Phys* 75:473–541.
2. Armitage NP, Fournier P, Greene RL (2010) Progress and perspectives on electron-doped cuprates. *Rev Mod Phys* 82:2421–2487.
3. Armitage NP (2001) Doping the copper-oxygen planes with electrons: The view with photoemission. PhD thesis (Stanford University, Stanford, CA).
4. Armitage NP, et al. (2002) Doping dependence of an n-type cuprate superconductor investigated by angle-resolved photoemission spectroscopy. *Phys Rev Lett* 88:257001.
5. Matsui H, et al. (2005) Angle-resolved photoemission spectroscopy of the antiferromagnetic superconductor $Nd_{1.87}Ce_{0.13}CuO_4$: Anisotropic spin-correlation gap, pseudogap, and the induced quasiparticle mass enhancement. *Phys Rev Lett* 94:047005.
6. Matsui H, et al. (2007) Evolution of the pseudogap across the magnet-superconductor phase boundary of $Nd_{2-x}Ce_xCuO_4$. *Phys Rev B* 75:224514.
7. Matsui H, et al. (2005) Direct observation of a nonmonotonic $d_{x^2-y^2}$ wave superconducting gap in the electron-doped high-Tc superconductor $Pr_{0.89}LaCe_{0.11}CuO_4$. *Phys Rev Lett* 95:017003.
8. Park SR, et al. (2007) Electronic structure of electron-doped $Sm_{1.86}Ce_{0.14}CuO_4$: Strong pseudogap effects, nodeless gap, and signatures of short-range order. *Phys Rev B* 75: 060501(R).
9. Armitage NP, et al. (2001) Anomalous electronic structure and pseudogap effects in $Nd_{1.85}Ce_{0.15}CuO_4$. *Phys Rev Lett* 87:147003.
10. Santander-Syro AF, et al. (2011) Two-Fermi-surface superconducting state and a nodal d-wave energy gap of the electron-doped $Sm_{1.85}Ce_{0.15}CuO_{(4-\delta)}$ cuprate superconductor. *Phys Rev Lett* 106:197002, and erratum (2011) 107:079901.
11. Ikeda M, et al. (2009) Effects of chemical pressure on the Fermi surface and band dispersion of the electron-doped high-T_c superconductors. *Phys Rev B* 80:014510.
12. Helm T, et al. (2009) Evolution of the Fermi surface of the electron-doped high-temperature superconductor $Nd_{2-x}Ce_xCuO_4$ revealed by Shubnikov-de Haas oscillations. *Phys Rev Lett* 103:157002.
13. Helm T, et al. (2010) Magnetic breakdown in the electron-doped cuprate superconductor $Nd_{2-x}Ce_xCuO_4$: The reconstructed Fermi surface survives in the strongly overdoped regime. *Phys Rev Lett* 105:247002.
14. Kartsovnik MV, et al. (2011) Fermi surface of the electron-doped cuprate superconductor $Nd_{2-x}Ce_xCuO_4$ probed by high-field magnetotransport. *New J Phys* 13:015001.
15. Helm T, et al. (2015) Correlation between Fermi surface transformations and superconductivity in the electron-doped high-Tc superconductor $Nd_{2-x}Ce_xCuO_4$. *Phys Rev B* 92:094501.
16. Breznay NP, et al. (2016) Shubnikov-de Haas quantum oscillations reveal a reconstructed Fermi surface near optimal doping in a thin film of the cuprate superconductor $Pr_{1.86}Ce_{0.14}CuO_{4\pm\delta}$. *Phys Rev B* 94:104514.
17. Higgins JS, et al. (2018) Quantum oscillations from the reconstructed Fermi surface in electron-doped cuprate superconductors. *New J Phys* 20:043019.
18. Dagan Y, Qazilbash MM, Hill CP, Kulkarni VN, Greene RL (2004) Evidence for a quantum phase transition in $Pr_{2-x}Ce_xCuO_{4-\delta}$ from transport measurements. *Phys Rev Lett* 92:167001.
19. Zhang X, et al. (2016) Transport anomalies and quantum criticality in electron-doped cuprate superconductors. *Physica C* 525–526:18–43.
20. Song D, et al. (2017) Electron number-based phase diagram of $Pr_{1-x}LaCe_xCuO_{4-\delta}$ and possible absence of disparity between electron- and hole-doped cuprate phase diagrams. *Phys Rev Lett* 118:137001.
21. Horio M, et al. (2018) Common origin of the pseudogap in electron-doped and hole-doped cuprates governed by Mott physics. arXiv:1801.04247.
22. Yu W, Higgins JS, Bach P, Greene RL (2007) Transport evidence of a magnetic quantum phase transition in electron-doped high-temperature superconductors. *Phys Rev B* 76:020503(R).
23. Motoyama EM, et al. (2007) Spin correlations in the electron-doped high-transition-temperature superconductor $Nd_{2-x}Ce_xCuO_{4+/-\delta}$. *Nature* 445:186–189.
24. Jin K, Butch NP, Kirshenbaum K, Paglione J, Greene RL (2011) Link between spin fluctuations and electron pairing in copper oxide superconductors. *Nature* 476:73–75.
25. Butch NP, Jin K, Kirshenbaum K, Greene RL, Paglione J (2012) Quantum critical scaling at the edge of Fermi liquid stability in a cuprate superconductor. *Proc Natl Acad Sci USA* 109:8440–8444.
26. Tafti FF, et al. (2014) Nernst effect in the electron-doped cuprate superconductor $Pr_{2-x}Ce_xCuO_4$: Superconducting fluctuations, upper critical field H_{c2}, and the origin of the T_c dome. *Phys Rev B* 90:024519.
27. Saadaoui H, et al. (2015) The phase diagram of electron-doped $La_{2-x}Ce_xCuO_{4-\delta}$. *Nat Commun* 6:6041.
28. da Silva Neto EH, et al. (2015) Charge ordering in the electron-doped superconductor $Nd_{2-x}Ce_xCuO_4$. *Science* 347:282–285.
29. Scheurer MS, et al. (2018) Topological order in the pseudogap metal. *Proc Natl Acad Sci USA* 115:E3665–E3672.
30. Sachdev S (2019) Topological order and Fermi surface reconstruction. *Rep Prog Phys* 82:014001.
31. Wu W, et al. (2018) Pseudogap and Fermi-surface topology in the two-dimensional Hubbard model. *Phys Rev X* 8:021048.